



ORIGINAL RESEARCH ARTICLE

# Investigation of Two Laser Heat Treatment Strategies for Local Softening of a Sheet in Age-Hardening Aluminum Alloy by Means of Physical Simulation

Maria Emanuela Palmieri and Luigi Tricarico

Submitted: 21 October 2023 / Revised: 13 March 2024 / Accepted: 28 March 2024

Car manufacturers increasingly aid high-strength aluminum alloys for their advantageous weight-to-strength ratio, but their limited formability poses challenges in plastic deformation processes. Tailored heat-treated blanks (THTBs) are a propitious approach to improve formability. Surface laser treatment is the predominant technology for obtaining THTB. To design this process quickly and accurately, without material waste, the use of physical simulation is increasingly promising. It allows replicating the process on a lab-scale and studying posttreatment mechanical and metallurgical properties. By adopting Gleeble® physical simulator, this study investigates the softening effects of local surface laser heat treatment on a EN AW 6082 T6 aluminum alloy blank. Two laser movement strategies—single linear path and multiple rectangular paths—were investigated at two treatment speeds for each. A finite element (FE) model was developed for simulating the process under all explored conditions. FE-derived thermal cycles were reproduced by means of physical simulation. After physical tests, alloy mechanical properties were evaluated. Results show that these properties depend on both the peak temperature thermal cycle and the interaction time between the laser source and the material surface. The comparison between the two strategies revealed that the multiple rectangular paths strategy allows to achieve a wider softened area at comparable interaction times.

**Keywords** laser material processing, numerical simulation, physical simulation, precipitation strengthen/hardened aluminum alloys, tailored heat-treated blanks

## 1. Introduction

Nowadays, in the mobility field, the key concepts are the vehicle's lightweighting and greater safety for passengers. To meet these requirements, high-strength aluminum alloys are increasingly being used. However, these aluminum alloys have low formability limits (Ref 1) which make forming and/or joining operations complex. To overcome this problem, before plastic deformation operations, local heat treatment can be carried out with the aim of softening the alloy. When the heat treatment is performed on the blanks before the stamping process, the blanks are defined tailored heat-treated blanks (THTBs) (Ref 1, 2). When the heat treatment is performed on a semi-finished product to facilitate joining operations, these components are defined as tailor heat-treated profiles (THTPs) (Ref 3, 4).

The main idea behind the use of localized heat treatments involves introducing a distribution of strength and ductility to the blank, optimized for subsequent plastic deformation steps.

For instance, tailor heat-treated blanks are commonly employed in constructing the body-in-white parts. Through the integration of both hard and soft regions into parts, it is possible to ensure both high strength, crucial for meeting safety criteria, and good formability.

Different heating technologies can be used to perform local heat treatment such as laser radiation, electromagnetic induction and heat conduction by heated contact plates (Ref 5-7). The most widely used technology is laser radiation, owing to its flexibility (Ref 1) and a broad range of applications. In addition to improving the local formability of the material, it can be used both for alloying to enhance surface properties (Ref 8) and for improving optical properties (Ref 9).

M. Graser et al. (Ref 10) adopted the laser heat treatment on EN AW 7075 T6 aluminum alloy to improve the joining process with 22MnB5 steel. N. Peixinho et al. (Ref 11) used the localized laser induced heat treatment for improving the forming behavior of aluminum EN AW 6063 T6 parts. A. Hetzel et al. (Ref 12) investigated the local laser heat treatment for increasing the forming limit of orbital formed tailored blank in EN AW 6016 aluminum alloy. S. Zarini et al. (Ref 13) studied a fiber laser heat treatment for enhancing the formability on EN AW 6060 T4 aluminum alloy and compared this technique with a furnace annealing.

Most of the scientific works about the local laser heat treatment investigated the age-hardened aluminum alloys that are the most attractive aluminum alloy for the transport industry due to their high strength (Ref 14). On age-hardened aluminum alloys, the softening after a local heat treatment by laser radiation is due to the dissolution of precipitates (Ref 15).

Maria Emanuela Palmieri and Luigi Tricarico, Dipartimento di Meccanica Matematica e Management, Politecnico di Bari, Bari, Italy. Contact e-mail: mariaemanuela.palmieri@poliba.it.

The research on the local laser heat treatment is still open. Recently, different local laser heat treatment strategies were investigated with the aim of optimizing the process (Ref 12, 16) and/or limiting distortion problems (Ref 17). In the literature, three irradiation strategies have been extensively explored: (i) the spotwise strategy (SW), which involves keeping the laser spot stationary within the treated area for a specified duration; (ii) the single linear path strategy (SLP), entailing the movement of the laser source along a single linear trajectory; and (iii) the multipath strategy (MP), wherein the laser source is moved along a defined path, creating multiple trajectories that can be either linear or have a predefined shape.

Rigas et al. (Ref 17) compared the spotwise strategy with the single linear path strategy, demonstrating that the latter facilitates a more rapid heating of components. However, the single linear path strategy results in greater distortion. Palmieri et al. (Ref 18) also conducted a comparison between these two strategies on a work-hardened aluminum alloy, EN AW 5754, revealing that the single linear path strategy ensures a higher level of softening compared to the spotwise strategy. Mohammadi et al. (Ref 19) compared the single-path strategy with the multipath strategy regarding their influence on bending properties, demonstrating that using a scanning strategy with a triple path reduced the springback issue after the bending operation. Finally, Rigas et al. (Ref 20) compared the single linear path strategy with the linear multipath strategy, observing that the latter ensures less distortion.

Performing experimental tests for these studies can involve high costs and significant material waste. Consequently, there's a rising trend in adopting physical simulation to replicate industrial processes on a laboratory scale. Several scientific works have embraced physical simulation for reproducing laser thermal cycles, which are critical due to their high heating and cooling rate (Ref 18, 21-24). Specifically, Palmieri et al. (Ref 18) showcased the reliability of such tests type, showing the congruence between results obtained from physically simulated samples and those treated with a laser source.

By adopting FE modeling and physical simulation tests, this study explores the influence of laser heat treatment strategy and process parameters on the softening level of the treated area of a blank in EN AW 6082 T6 aluminum alloy with a thickness equal to 1 mm.

For this purpose, two different treatment strategies were investigated, the single linear path strategy and what will be referred to as multiple rectangular path (MRP), where the laser source moves, drawing a rectangular paths. This latter strategy was examined to assess its potential in extending interaction times and achieving a greater softening effect on the material compared to the conventional SLP strategy. The objective is to compare these two strategies in terms of the achieved level of softening, peak temperature ensuring maximum softening, and the extent of the softened zone.

## 2. Material and Method

For this study, the investigated alloy is the EN AW 6082 T6 age-hardened aluminum alloy. The chemical analysis and the mechanical properties in the supply state are listed in Tables 1 and 2, respectively. Scheme of the two investigated laser heat treatment strategies: (a) single linear path and (b) multiple rectangular paths

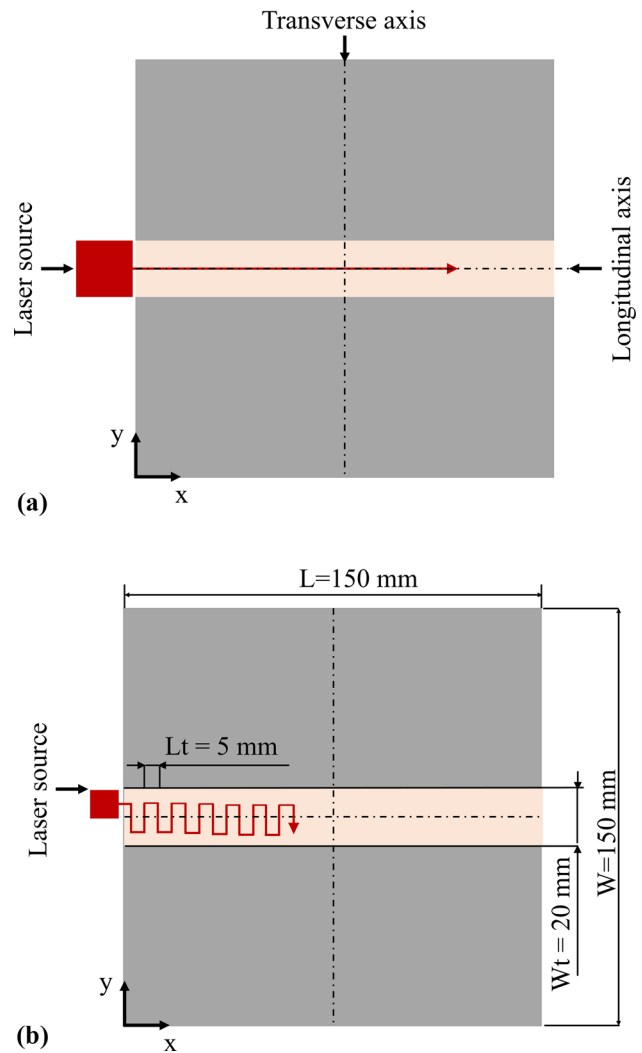


**Fig. 1** Scheme of the two investigated laser heat treatment strategies: (a) single linear path and (b) multiple rectangular paths

**Table 1** Chemical analysis of the EN AW 6082 T6 aluminum alloy (Ref 25)

Si	Fe <sup>2</sup>	Cu	Mn	Mg	Al
0.7-1.3	≤ 0.5	≤ 0.1	0.4-1	0.6-1.2	balanced

The aim of this study is to investigate the effects of laser heat treatment using two different strategies for laser source movement on the softening of this alloy.

Through a finite element (FE) model developed in Comsol<sup>®</sup> Multiphysics, laser heat treatments were simulated on a sheet metal section with overall dimensions of 150 × 150 mm, restricting the treated area to 150 × 20 mm. The two different laser source movement strategies are schematically illustrated in Fig. 1.

Figure 1(a) illustrates the SLP strategy, while Fig. 1(b) depicts the MRP strategy. Two different treatment speeds were explored for each strategy, resulting in a total of four laser heat treatments condition investigated. For all the investigated laser

**Table 2 Mechanical properties of the EN AW 6082 T6 aluminum alloy (Ref 25)**

Tensile strength, MPa	Yield strength, MPa	Elongation at break $A_{50}$ , %	Hardness, HV
310 MPa	260 MPa	10	110

treatment conditions, the FE model allowed for the extraction of thermal cycles to be reproduced on a laboratory scale. These cycles were obtained at the center point of the treated blank. Furthermore, the developed FE model enabled the analysis of the temperatures distribution on the blank during the laser surface treatment. The thermal cycles derived from FE model were then reproduced on a laboratory scale using the Gleeble®3180 physical simulator.

After physical simulation tests, the specimens were subjected to hardness and tensile tests after a 144-hour period (close to natural aging conditions—state T4). The mechanical characterization tests were conducted assuming that, on an industrial scale, blanks that undergo local softening can be used for plastic forming operations at a later stage. In this step, the laser treatment condition that ensures the maximum softening condition was identified.

Finally, the FE model was used to simulate the laser heat treatment in the maximum softening condition and determine, in this condition, the peak temperatures in the blank during the process. The peak temperatures were evaluated on a grid of points defined on the blank surface.

The experimental hardness results were correlated with these peak temperatures to compare SLP and MRP strategies in terms of width and uniformity of softened area. The uniformity of peak temperatures and hardness along the treatment direction was guaranteed by varying the laser power, so as to maintain stationary conditions over the entire treated surface.

### 3. FE Model of Laser Heat Treatment Strategies

A transient three-dimensional thermal model was developed using the FE software COMSOL Multiphysics 5.6 to numerically simulate the localized laser heat treatments. The laser heat treatments were modeled assuming treatment of a portion of an aluminum alloy blank, specifically EN AW 6082, with overall dimensions of  $150 \times 150$  mm and a thickness of 1 mm.

In the SLP strategy, a laser source with a square spot size of  $20 \times 20$  mm maintains a constant treatment speed ( $V_t$ ) along the longitudinal section of the blank (Fig. 1a). In the MRP strategy, the laser source with a square spot size  $10 \times 10$  mm moves with a constant  $V_t$  by following the trajectory shown in Fig. 1b. Specifically, the laser source advances first in the longitudinal direction of the blank by 5 mm ( $L_t$ ), and then moves in the transverse direction to cover the entire width of the treated area ( $W_t$ ), which is 20 mm. This movement is repeated to cover the entire length of the blank, measuring 150 mm. The laser spot overlap between adjacent paths was set equal to 5 mm.

The coordinates for the movement of the laser source were assigned in the FE model. The laser spot size in MRP treatment is smaller than in SLP treatment so that the width of the treated area is equivalent for both treatments.

**Table 3 Process parameters of the investigated laser heat treatments**

Treatment code	SLP		MRP	
	SLP-Vt5	SLP-Vt10	MRP-Vt10	MRP-Vt50
$V_t$ , mm/s	5	10	10	50
$P_L$ , kW	0.65	0.44	0.675	1.35

The process parameters, i.e., treatment speed and absorbed laser power ( $P_L$ ), used for this study are listed in Table 3.

The laser power value was chosen aiming to achieve a uniform peak temperature of approximately 500 °C in the treated area. The absorbed laser power was calibrated to assure a steady-state condition during the surface treatment, i.e., thermal cycles with a constant peak temperature. For the calibration, some probes were positioned on the blank surface along the blank length.

In the laser heat treatment with the MRP strategy, the equivalent speed ( $V_{eq}$ ) was calculated, which represents the speed that the laser would take to treat a blank portion of length  $L_x$  if a laser heat treatment with the SLP strategy was performed. The equivalent speed is equal to 2 mm/s in the MRP-Vt10 treatment and 10 mm/s in the MRP-Vt50 treatment.

In the developed FE model, the heat transfer problem is governed by the Eq 1:

$$\rho c_p \frac{\partial T}{\partial t} = \text{div} \left( \overrightarrow{k \text{grad}(T)} \right) \quad (\text{Eq 1})$$

where  $\rho$ ,  $c_p$  and  $k$  are, respectively, the density, specific heat, and thermal conductivity of the material, while  $T$  is the temperature, and  $t$  is the time. The thermophysical material properties were modeled as a function of temperature, as highlighted in Table 4.

The heat generated by laser-material interaction ( $Q_{\text{laser}}$ ) was modeled as a surface heat source with a top hat distribution, according to the Eq 2:

$$Q_{\text{laser}} = \frac{P_L}{4a_x a_y} \times I_{\text{laser}} \quad (\text{Eq 2})$$

where  $P_L$  is the absorbed laser power,  $I_{\text{laser}}$  is the top hat distribution function, and  $a_x$  and  $a_y$  are the laser square spot size. As the laser spot is square, both  $a_x$  and  $a_y$  have equal values. In the SLP treatment, these parameters are set to 20 mm, while in the MRP treatment, they are equal to 10 mm.

The FE model utilizes a suitably refined mesh in the area affected by major thermal gradients. In the fine mesh zone, a hexahedron (brick) element type with a mapped square mesh is adopted, where the maximum element size in the plane is 1 mm and there are three elements in the sheet thickness. In the coarse mesh region, an unstructured mesh is used.

**Table 4 Functions of thermophysical properties ( $\rho$ ,  $c_p$ ,  $k$ ) (Ref 26)**

$T, ^\circ\text{C}$	$k, \text{W, mK}$	$c_p, \text{J, kg K}$	$\rho, \text{kg, m}^3$
20-600	$182.2 + 0.06 T$	$893.7 + 0.6 T$	$(2.8 \cdot 2 \times 10^{-4} T) \times 1/10^{-6}$

In the laser-material interaction zone, a heat transfer coefficient of  $15 \text{ W}/(\text{m}^2\text{K})$  is assumed, taking into account the action of the shielding gas. This value has been calibrated based on the experimental tests described in a previous work by the authors (Ref 18).

### 3.1 Experimental Procedure

For the physical simulation of the laser thermal cycles, notched specimens were adopted in order to respect the high cooling rates (Ref 18, 21). These specimens have a total length of 150 mm and a width of 35 mm. The tapered area has a width equal to 10 mm and a length equal to 20 mm, with a fillet radius of 3 mm (Fig. 2a). The experimental setup for physical simulation tests is shown in Fig. 2b.

Four K-type thermocouples (TC1, TC2, TC3, and TC4) were welded onto the specimens. The thermocouple TC1 was welded in the center of the specimen. The others were welded at a distance of about 5, 15, and 25 mm from the centre, respectively. Thermocouple TC1 is set as the pilot thermocouple. Based on the temperature acquired by this thermocouple, a closed-loop feedback controller modulates the current density to heat, by Joule effect, the specimen to the set temperature. As can be seen in Fig. 2a, the specimen is horizontally held between copper grips inserted inside water-cooled jaws. Due to the operating principle of the Gleeble system, a thermal gradient develops along the longitudinal axis of the specimen during the physical simulation tests.

After physical simulation tests, the specimens were subjected to natural aging (144 h) and then to microhardness, tensile tests, and metallographic analysis.

Hardness measurements were performed along the longitudinal axis of the specimen with a load of 0.2 kg and a dwell time of 15 s. The distance between the indentations was set at 1 mm.

For the tensile tests, the specimens were machined to produce a notch in the middle section. This geometry promotes the localization of deformation at the point where the pilot thermocouple was welded, i.e., at the point subjected to the set thermal cycle. The tensile tests were performed with a moving crosshead speed ( $v$ ) of 10 mm/min. In order to be able to assess the deformations locally, the tensile tests were assisted by a digital image correlation (DIC) system. For this purpose, the specimens were covered with an opaque white paint, and then a random black dot pattern was created.

Metallographic observations were carried out with Zeiss Supra 35 scanning electron microscopy (SEM) using back scattered electrons (BSD). Moreover, BSD detector was coupled to an energy-dispersive spectroscopy (EDS) for chemical analysis of precipitates. Samples for SEM investigation were polished by means of active oxide polishing (OP-S) suspension (colloidal silica suspension).

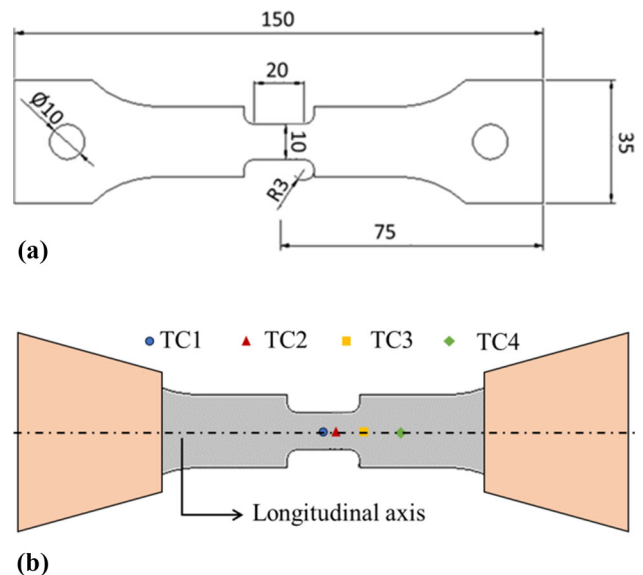


**Fig. 2** (a) Specimen geometry and (b) experimental setup for physical simulation test

## 4. Results and Discussion

### 4.1 Numerical Results: Thermal Cycles and Peak Temperatures Distribution on the Blank

In the FE model, some probes were defined on the blank surface, the central one was used to obtain the thermal cycles corresponding to the laser treatment conditions specified in Table 3. Figure 3 illustrates these thermal cycles, with Fig. 3(a) representing the cycles for the SLP strategy, and Fig. 3(b) displaying the cycles for the MRP strategy.

Increasing the treatment speed leads to a more rapid thermal cycle, resulting in less time for the blank to remain at high temperatures. This time is defined as the interaction time ( $\tau$ ), and it can be calculated as the ratio between the laser spot size and the treatment speed (Ref 27, 28) in the SLP strategy. In the other strategy, it is defined as the ratio between the laser spot size and the equivalent speed.

The interaction time is 4 s and 2 s for the SLP-Vt5 and SLP-Vt10 treatments, respectively. In contrast, for the MRP-Vt10 and MRP-Vt50 treatments,  $\tau$  parameter is equal to 5 s and 1 s, respectively. As expected, a lower treatment speed results in a longer interaction time. The SLP-Vt5 and MRP-Vt10 treatments have a comparable interaction time, differing by 1 s. The same applies to the SLP-Vt10 and MRP-Vt50 treatments.

The FE model allowed an analysis of the temperature distribution in the blank during the process.

As an example, Fig. 4(a) displays the temperature distribution for SLP treatment at  $V_t=5 \text{ mm/s}$ , and Fig. 4(b) shows the temperature distribution for MRP treatment at  $V_t=10 \text{ mm/s}$ .

### 4.2 Experimental Results: Hardness and Tensile Tests

As described in Section 2, the thermal cycles acquired from the FE model were experimentally reproduced on 1 mm thick 6082 T6 aluminum alloy specimens. For some of the laser heat treatment conditions investigated, Fig. 5 shows the thermal cycles acquired by the thermocouples welded along the longitudinal axis of the specimen. Specifically, Fig. 5(a) shows

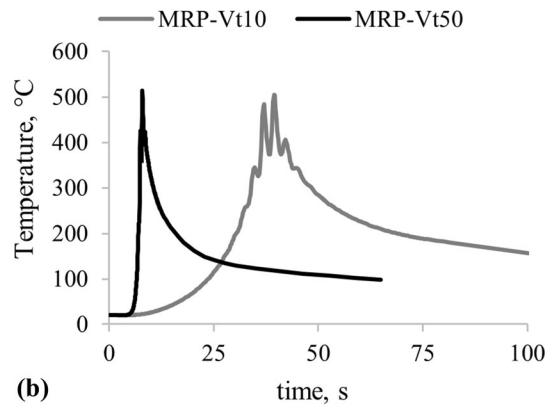
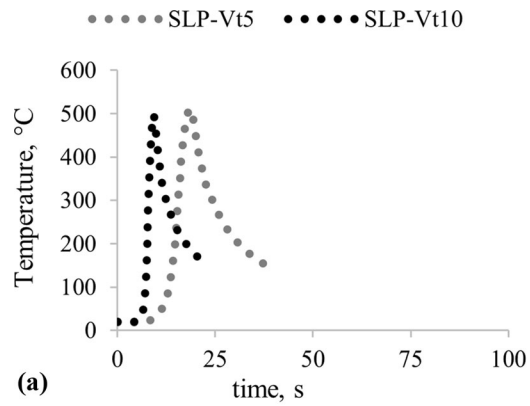


**Fig. 3** Thermal cycles of laser treatments for (a) the SLP strategy and (b) the MRP strategy

the results for laser heat treatment with a single linear path carried out at  $V_t=10$  mm/s. Figure 5(b) shows the results for laser heat treatment with multiple rectangular paths carried out at  $V_t=10$  mm/s. For the same laser heat treatment conditions, Fig. 6 shows, with the markers, the peak temperatures ( $T_{peak}$ ) acquired by the thermocouples as a function of the distance from the specimen center ( $x$ ). Tables 5 and 6 show the polynomials adopted to fit  $T_{peak}$  versus  $x$  for all laser heat treatment condition explored. In detail, Table 5 reports on the polynomials for single linear path laser heat treatment, and Table 6 for multiple rectangular paths laser heat treatment.

For distances greater than 15 mm from the center of the specimen, as observed from the graphs in Fig. 6, the peak temperature drops below 300 °C. At such low peak temperatures, no great softening effects occur, as will be discussed later. For this reason, a first-order linear equation was used to approximate the peak temperature as a function of the distance from specimen center for  $x > 15$  mm.

From the graphs in Fig. 5 and Fig. 6, it can be seen that the temperature decreases moving from the pilot thermocouple (TC1) to the thermocouple closest to the cold grip (TC4). In the first 25 mm, the peak temperature ranges from a maximum of 500 °C to a minimum of around 200 °C. As demonstrated by Palmieri et al. (Ref 18), a single physical simulation test is able to reproduce laser thermal treatments made with the same strategy (single path or multiple rectangular paths), with the same treatment speed, but with laser powers lower, i.e., lower peak temperature than that corresponding to the control point.

Hardness measurements along the longitudinal axis of the specimen are shown in Fig. 7(a).

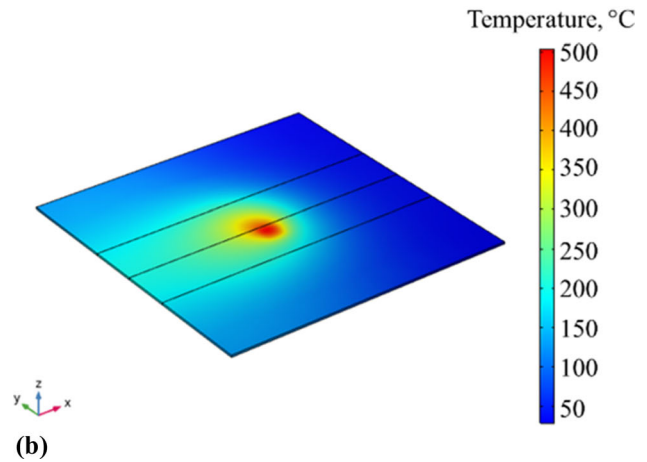
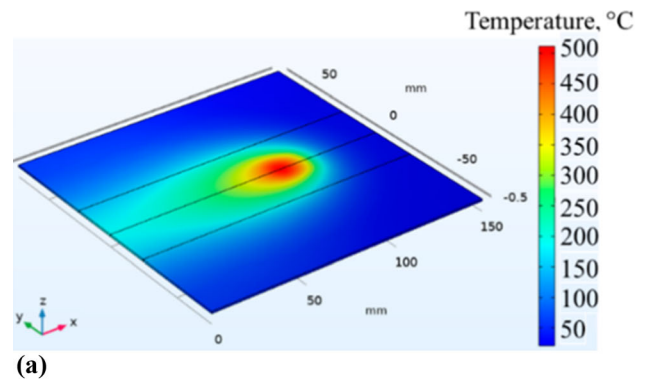


**Fig. 4** Temperature distribution in the blank for laser heat treatments (a) SLP-Vt5 and (b) MRP-Vt10

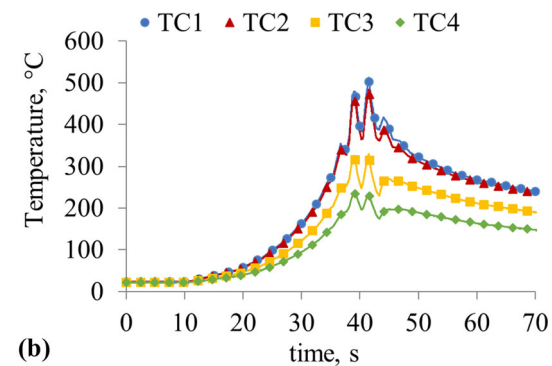
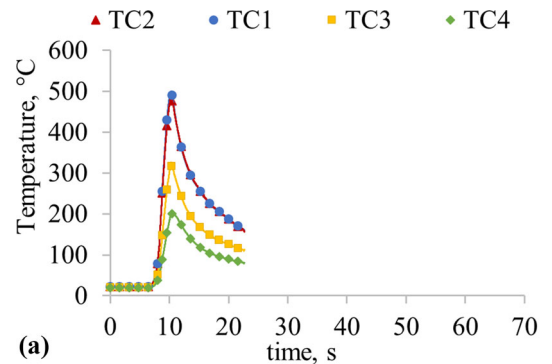


**Fig. 5** Thermal cycles acquired from thermocouples welded along the longitudinal axis of the specimen in the case of laser heat treatment (a) SLP-Vt10 and (b) MRP-Vt10

Starting from the specimen centre, it is observed that, for all the laser conditions investigated, the hardness first decreases to a minimum value and then rises to the value in the supplied state. The hardness profile exhibits a W-shape, and it is symmetrical with respect to the specimen center.

The trend of the hardness as a function of distance from the specimen center is justified by the temperature distribution during the physical simulation test. Using the polynomials in Tables 5 and 6, it is possible to plot the graph of hardness versus peak temperature (Fig. 7b).

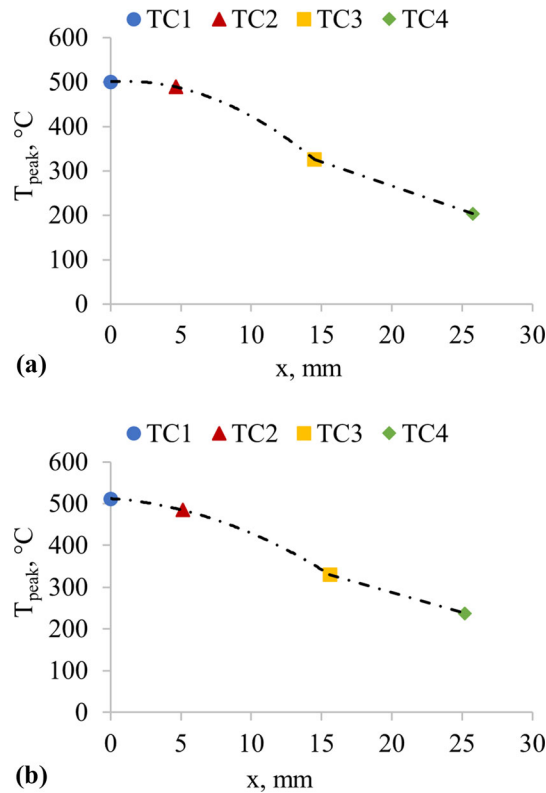


**Fig. 6** Peak temperatures acquired from thermocouples welded along the longitudinal axis of the specimen during physical simulation tests of (a) SLP-Vt10 and (b) MRP-Vt10

**Table 5** Polynomials fitting the experimental data of peak temperatures as a function of distance from the specimen center for the laser heat treatments with single linear path

	SLP-Vt5	SLP-Vt10
$0 < x \leq 15$ mm	$T_{peak} = -0.66 \times x^2 - 2.27 \times x + 509$	$T_{peak} = -0.97 \times x^2 + 1.97 \times x + 510.5$
$x > 15$ mm	$T_{peak} = -10.36 \times x + 510.5$	$T_{peak} = -10.9 \times x + 484$

**Table 6** Polynomials fitting the experimental data of peak temperatures as a function of distance from the specimen center for the laser heat treatments with multiple rectangular paths

	MRP-Vt10	MRP-Vt50
$0 < x \leq 15$ mm	$T_{peak} = -0.6 \times x^2 - 2.4 \times x + 512$	$T_{peak} = -0.89 \times x^2 - 3.05 \times x + 510.7$
$x > 15$ mm	$T_{peak} = -9.7 \times x + 482.4$	$T_{peak} = -8.92 \times x + 408.9$

It is observed that for peak temperatures below 200 °C, the hardness remains constant and equal to the hardness value of the alloy in the as-supplied state. For peak temperatures above 200 °C and up to peak temperatures ranging between 410 °C-430 °C, the hardness decreases. For peak temperatures exceeding 410 °C-430 °C, the hardness increases, although it always remains lower than that of the T6 state of the alloy. The peak temperature range between 410 °C-430 °C therefore allows the maximum softening for the alloy and for the strategies and process parameters investigated.

From the graphs in Fig. 7, it is evident that peak temperature is not the only parameter influencing the alloy hardness, particularly for high peak temperatures. The other parameter is the treatment speed and, consequently, the interaction time.

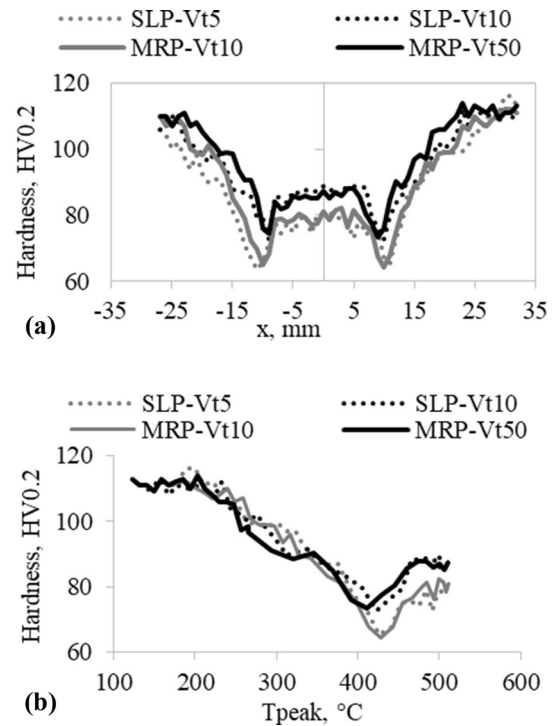


**Fig. 7** Hardness trend (a) as a function of the distance from the specimen center and (b) as a function of the peak temperature

**Table 7. Polynomials for fitting the hardness data as a function of peak temperature for all investigated laser heat treatments**

	SLP-Vt5	R <sup>2</sup>
$T_{\text{peak}} \leq 200 \text{ }^\circ\text{C}$	HV0.2 = 110	0.99
$200 \text{ }^\circ\text{C} < T_{\text{peak}} \leq 410 \text{ }^\circ\text{C}$	$\text{HV0.2} = -7 \times 10^{-6} (T_{\text{peak}})^3 + 0.006 (T_{\text{peak}})^2 - 1.9 T_{\text{peak}} + 307.9$	0.9
$410 \text{ }^\circ\text{C} < T_{\text{peak}} \leq 490 \text{ }^\circ\text{C}$	$\text{HV0.2} = -9 \times 10^{-5} (T_{\text{peak}})^3 + 0.12 (T_{\text{peak}})^2 - 56.2 T_{\text{peak}} + 8611.5$	0.9
$490 \text{ }^\circ\text{C} < T_{\text{peak}} \leq 500 \text{ }^\circ\text{C}$	HV0.2 = 79	0.99
<i>SLP-Vt10</i>		
$T_{\text{peak}} \leq 200 \text{ }^\circ\text{C}$	HV0.2 = 110	0.99
$200 \text{ }^\circ\text{C} < T_{\text{peak}} \leq 405 \text{ }^\circ\text{C}$	$\text{HV0.2} = 2 \times 10^{-6} (T_{\text{peak}})^3 - 0.001 (T_{\text{peak}})^2 + 0.205 T_{\text{peak}} + 113.4$	0.97
$405 \text{ }^\circ\text{C} < T_{\text{peak}} \leq 490 \text{ }^\circ\text{C}$	$\text{HV0.2} = 2 \times 10^{-4} (T_{\text{peak}})^3 + 0.24 (T_{\text{peak}})^2 - 109 T_{\text{peak}} + 16485$	0.94
$490 \text{ }^\circ\text{C} < T_{\text{peak}} \leq 500 \text{ }^\circ\text{C}$	HV0.2 = 87	0.99
<i>MRP-Vt10</i>		
$T_{\text{peak}} \leq 200 \text{ }^\circ\text{C}$	HV0.2 = 110	0.99
$200 \text{ }^\circ\text{C} < T_{\text{peak}} \leq 410 \text{ }^\circ\text{C}$	$\text{HV0.2} = 5 \times 10^{-7} (T_{\text{peak}})^3 - 0.001 (T_{\text{peak}})^2 + 0.27 T_{\text{peak}} + 92.16$	0.94
$410 \text{ }^\circ\text{C} < T_{\text{peak}} \leq 490 \text{ }^\circ\text{C}$	$\text{HV0.2} = -2 \times 10^{-4} (T_{\text{peak}})^3 + 0.24 (T_{\text{peak}})^2 - 107 T_{\text{peak}} + 16175$	0.96
$490 \text{ }^\circ\text{C} < T_{\text{peak}} \leq 500 \text{ }^\circ\text{C}$	HV0.2 = 78	0.99
<i>MRP-Vt50</i>		
$T_{\text{peak}} \leq 200 \text{ }^\circ\text{C}$	HV0.2 = 110	0.99
$200 \text{ }^\circ\text{C} < T_{\text{peak}} \leq 405 \text{ }^\circ\text{C}$	$\text{HV0.2} = -8 \times 10^{-6} (T_{\text{peak}})^3 + 0.008 (T_{\text{peak}})^2 - 2.53 T_{\text{peak}} + 378.5$	0.94
$405 \text{ }^\circ\text{C} < T_{\text{peak}} \leq 490 \text{ }^\circ\text{C}$	$\text{HV0.2} = -7 \times 10^{-5} (T_{\text{peak}})^3 + 0.09 (T_{\text{peak}})^2 - 42.3 T_{\text{peak}} + 6259.8$	0.93
$490 \text{ }^\circ\text{C} < T_{\text{peak}} \leq 500 \text{ }^\circ\text{C}$	HV0.2 = 86	0.99

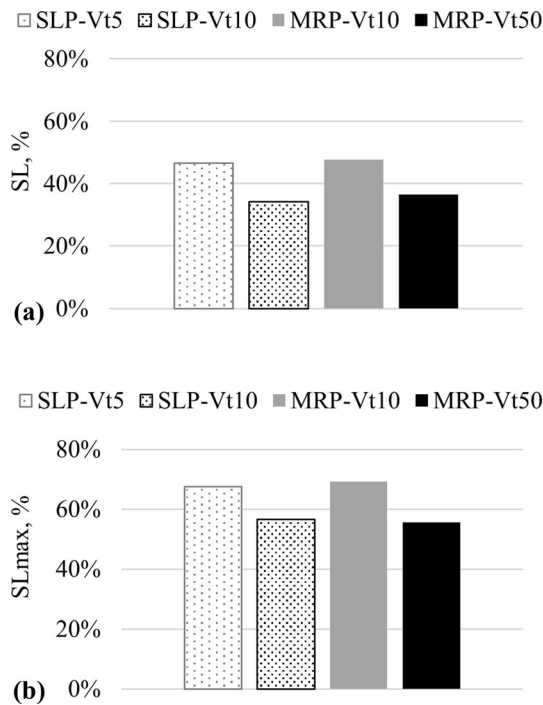


**Fig. 8** (a) Softening level achieved for laser conditions ensuring a peak temperature of 500 °C (b) and maximum softening level achieved for peak temperatures of 410 °C (SLP-Vt10, MRP-Vt50) and 430 °C (SLP-Vt5, MRP-Vt10)

Specifically, the shorter the interaction time, the higher the hardness value and then the lower is the softening level. The minimum hardness value is approximately 73 HV0.2 for the laser heat treatments SLP-Vt10 and MRP-Vt50, while it is around 64 HV0.2 for the laser heat treatments SLP-Vt5 and MRP-Vt10. Comparable softening differences are observed even at peak temperatures higher than those of maximum

softening. A reduction in the interaction time also shows a slight reduction in the peak temperature corresponding to the maximum softening. This temperature is about 410-420 °C for the SLP-Vt10 and MRP-Vt50 treatments, while it is around 430 °C for the SLP-Vt5 and MRP-Vt10 treatments.

The softening mechanisms observed in the EN AW 6082 T6 aluminum alloy under laser thermal cycles are similar to those occurring in the heat-affected zone (HAZ) of a welded joint. These mechanisms are well-documented in the literature (Ref 29, 30). T. Ma et al. (Ref 31), through welding simulations and experimental tests, demonstrated that the HAZ comprises a zone where hardness increase, and zone where hardness decreases. In the first zone, the increasing in hardness is due to the fact that dissolved precipitates reform into hardening precipitates during the natural aging. In the second zone, the overaging phenomenon causes the hardness decreases. Moreover, they showed that a higher thermal input, and consequently, longer interaction times, contribute to more significant softening and a wider softened area, positioned farther away from the fusion boundary. Similar results were obtained by Y. Liang et al. (Ref 32), who observed a softening mechanism arising from microstructural transformation in the HAZ, along with an increased width and reduced hardness with an increasing TIG current.

The softening observed above 200 °C and up to the temperature range from 410 °C to 430 °C is attributed to the overaging phenomenon, i.e., the increase in size of the Mg<sub>2</sub>Si phases, together with the transformation of these phases from the coherent form (β'') to the semi-coherent one (β'), up to the transformation of β' into the incoherent phase (β) corresponding to the equilibrium condition (Ref 33, 34). The increase in the peak temperature decreases the strengthening effect of these precipitates and the hardness reduction observed shows that the transformations just described are not complete and depend not only on the peak temperature but also on the time available for transformations, i.e., on the interaction time. With the increase of the interaction time, an ever greater volume fraction of

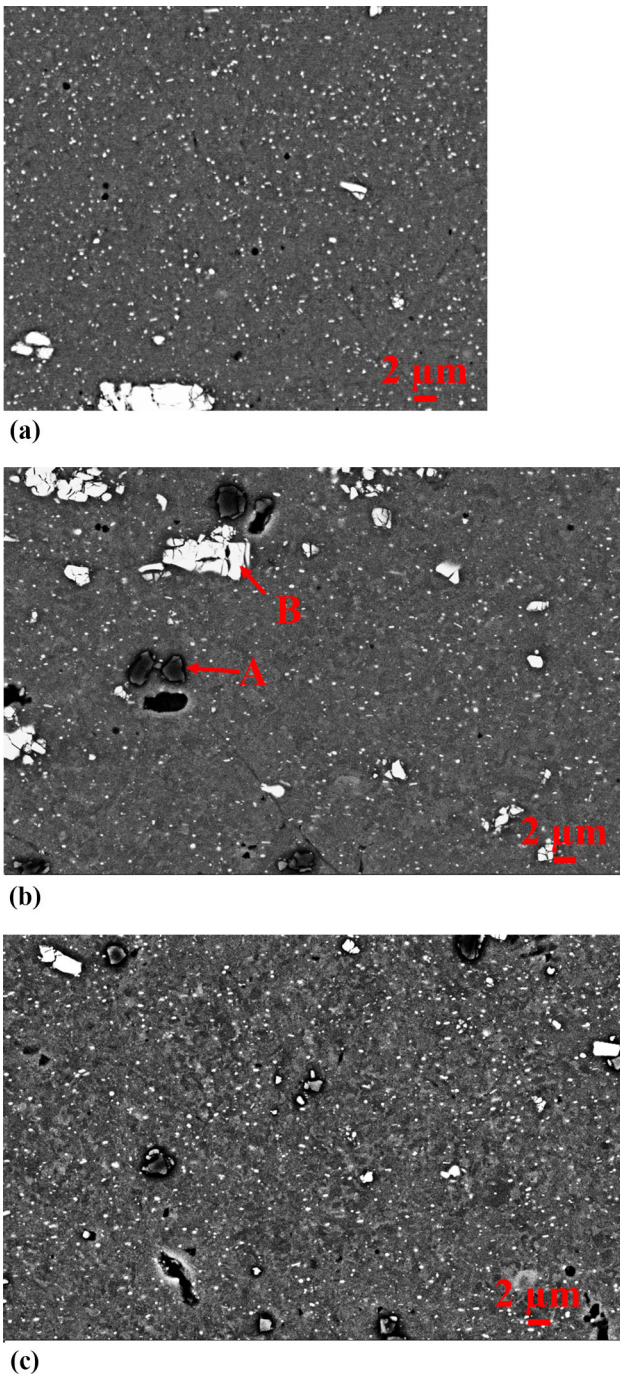


**Fig. 9** BSE-SEM image: (a) as-received material, (b) at 10 mm from the center of the specimen (maximum softening point) after the SLP-Vt5 cycle, and (c) at 9 mm from the center of the specimen (maximum softening point) after the SLP-Vt10 cycle

strengthening precipitates is involved in the transformations just described, increasing the level of softening obtained. Moreover, the softened zone becomes wider, as shown in Fig. 7(a), where the minimum hardness is farther from the center of the sample in the SLP-Vt5 and MRP-Vt10 treatments compared to the other two treatments.

For peak temperatures above that of maximum softening, part of the precipitates begins to dissolve in the  $\alpha$  solid solution of the alloy. The partial dissolution of the precipitates results in a reduction of their reinforcing effect, but the enrichment of the

solid solution also results in a strengthening of the alloy by solid solution. Furthermore, since the cooling rates of the laser thermal cycles are high, at ambient temperature the treated material is in a supersaturated solid solution, therefore susceptible to natural aging. The final effect is an increase in hardness with respect to that of maximum softening, which also in this case depends on the interaction time. Softening at the peak temperature of 500 °C decreases with decreasing interaction time due to the smaller amount of precipitates dissolving in the  $\alpha$  solid solution.

The curves in Fig. 7(b) were interpolated using the polynomials in Table 7.

The investigated laser heat treatments were compared in terms of softening. The level of softening of the alloy (SL) was calculated as in Eq 3.

$$SL = \frac{HV_{SS} - HV_{lht}}{HV_{SS} - HV_a} \quad (\text{Eq 3})$$

where  $HV_{SS}$  is the hardness of the alloy in the as-supplied state (110 HV),  $HV_{lht}$  is the hardness of the alloy naturally aged after the physical simulation of laser heat treatment, and  $HV_a$  is the alloy hardness after the complete annealing in a furnace. The annealing treatment was performed at a temperature of 500 °C for a duration of 20 minutes, and a hardness of  $44 \text{ HV}_{0.2} \pm 1$  was recorded.

Figure 8(a) displays histograms of the softening level of the alloy for all investigated laser heat treatments.

By replacing the value of  $HV_{lht}$  in Eq 1 with the minimum hardness value observed at peak temperatures of 410-430 °C, the histograms in Fig. 8(b) are obtained. These histograms represent the maximum softening level ( $SL_{max}$ ) of the alloy, i.e., the softening that would be achieved if the alloy underwent a treatment with a laser power guaranteeing peak temperatures of 410-430 °C.

As expected, it is observed that an increase in treatment speed results in a reduction of the softening level. In the conditions ensuring a peak temperature equal to 500 °C, this reduction is approximately 46% for the laser heat treatments SLP-Vt5 and MRP-Vt10. On the other hand, for the laser heat treatments SLP-Vt10 and MRP-Vt50, a lower softening level of approximately 35% is achieved.

Under the condition of maximum softening, the laser heat treatments SLP-Vt5 and MRP-Vt10 achieve a softening level of approximately 68%, while the SLP-Vt10 and MRP-Vt50 treatments achieve a softening level of approximately 56%.

From the histograms in Fig. 8(b), it is evident that the softening level cannot exceed 65%, confirming the literature's findings that laser-induced softening offers a lower level compared to full annealing in a furnace (Ref 35).

Following the hardness tests, metallographic analyses were conducted at locations where the minimum hardness was observed. In Fig. 9, micrographs showcase the as-received material (Fig. 9a) alongside those captured at the points of minimum hardness for samples treated with SLP-Vt5 (Fig. 9b) and SLP-Vt10 (Fig. 9c).

The BSE-SEM image highlights the presence of white and dark precipitates.

The EDS examination of the white precipitates indicates the existence of heavy elements, specifically Fe and Mn. As an example, Figure 10(a) displays the EDS analysis obtained at the point B highlighted in Fig. 9(b). Phases with substantial amounts of heavy elements exhibit a brighter appearance



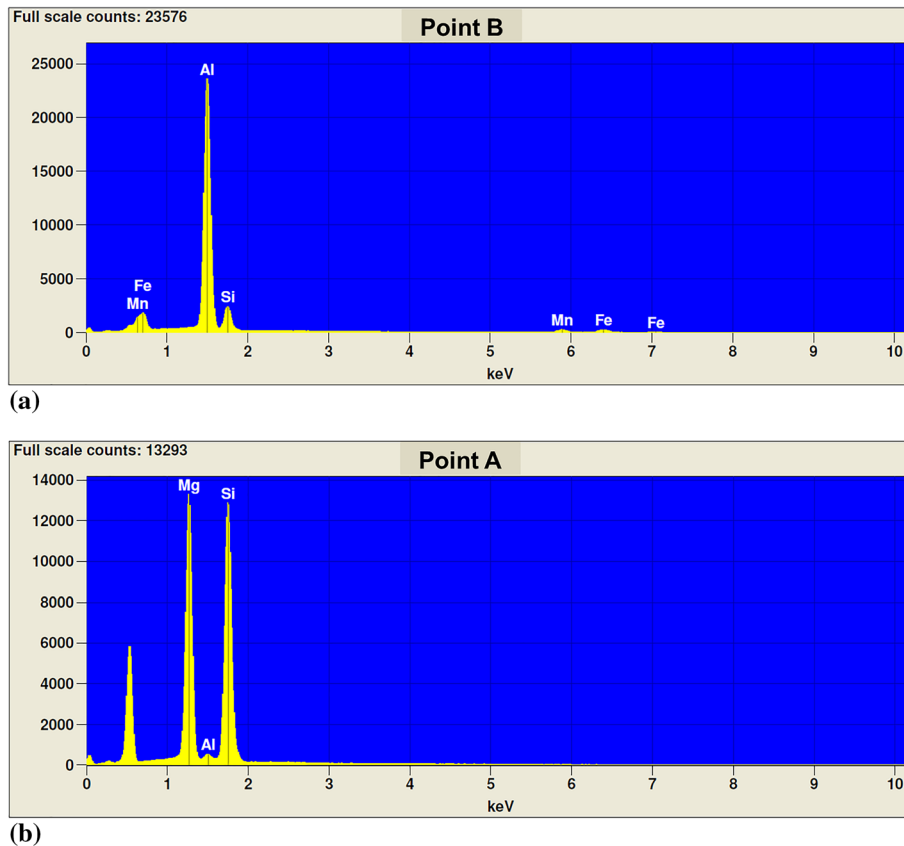


**Fig. 10** EDS analysis of (a) white precipitate-point B and (b) dark precipitate-point A

compared to those containing lighter elements. The introduction of Fe impurities in aluminum leads to the precipitation of a high fraction of coarse constituents rich in Fe and Si during the casting process (Ref 36). The large intermetallics observed in the micrographs form during material elaboration and do not contribute to alloy hardening (Ref 37). The white particles are consistently found in both the base material and the treated sample.

The darker precipitates are not visible in the as-received material but only in the treated specimens. The EDS examination of these dark precipitates unveils the existence of Mg and Si, which corresponds to the  $\beta$ -equilibrium precipitates. As an example, Figure 10(b) displays the EDS analysis obtained at the point A highlighted in Fig. 9(b). In the micrographs of the base material and treated specimens, the strengthening precipitates  $\beta'$  and  $\beta''$  are not visible due to their nanometric dimensions, which fall below the resolution of the SEM.

Through qualitative analysis, it is evident that an increase in treatment speed results in smaller dimensions of the  $\beta$  precipitates. This aligns with the lower interaction time at lower treatment speed.

Future analyses will involve the use of transmission electron microscopy (TEM) for a more in-depth examination of the  $\beta'$  e  $\beta''$  precipitates, aiming to correlate them with the adopted process parameters.

The results of the hardness tests were confirmed by tensile tests. The engineering stress-strain curves are shown in Fig. 11. These curves were obtained by evaluating the local deformation, specifically at the rupture point (Figure 11a).

Fig. 11(b) displays the curves obtained for the specimens subjected to the thermal cycles shown in Fig. 3.

The results show that all the laser treated specimens exhibit a lower ultimate tensile strength (UTS) and greater elongation at break (A) when compared to the material in the supply state. However, in comparison to the completely annealed state, the investigated laser treatments provide a lower A and greater UTS.

Furthermore, from the curves in Fig. 11(b), it can be observed that for both investigated strategies, an increase in the treatment speed leads to an increase in the ultimate tensile strength and a reduction in the elongation at break.

Consistent with the results of the hardness tests, the results in terms of UTS and A of the laser treatments with the SLP strategy are close to those obtained for the MRP strategy. This similarity occurs when the treatment speed of the MRP strategy is equivalent to that of the SLP one.

Specifically, the SLP-Vt5 and MRP-Vt10 laser treatments record a 17% lower ultimate tensile strength and a 14% higher elongation at break compared to the SLP-Vt10 and MRP-Vt50 laser treatments.

### 4.3 Investigation of the Maximum Softening Conditions

The hardness test results in section 3.3 reveal that longer interaction time, and consequently, a slower treatment speed, lead to higher levels of softening. Among the investigated laser conditions, the SLP-Vt5 and MRP-V10 treatments allow for greater softening. Anyway, the maximum softening occurs at a peak temperature of about 430 °C.

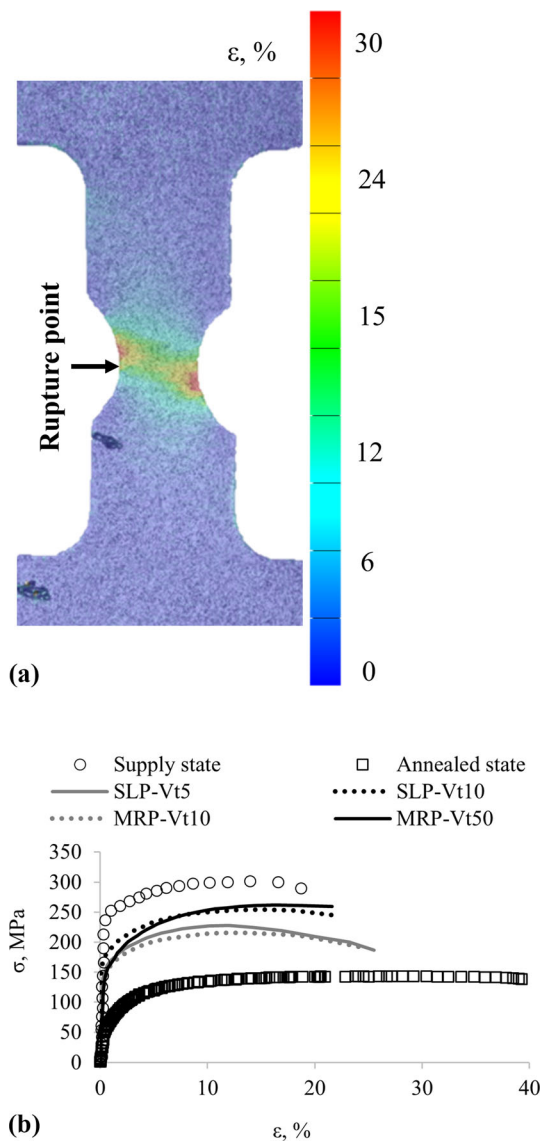


**Fig. 11** (a) Rupture point and (b) engineering stress-strain curves achieved for specimens at supply state, after furnace annealing and after physical simulation of laser thermal cycles SLP-Vt5 and MRP-Vt10 at a peak temperature of 500 °C

The FE model, described in section 2.1, was used to simulate the laser heat treatment that ensures the peak temperature of maximum softening (SLP-Vt5-MaximumSoftening and MRP-Vt10-MaximumSoftening). The corresponding FE thermal cycles, recorded at the center of the blank, are shown in Fig. 12 with the solid line.

The dashed lines in Fig. 12 represent the experimental thermal cycles acquired by welding a thermocouple at 10 mm from the specimen center during the physical simulation of SLP-Vt5 and MRP-Vt10 thermal cycles with peak temperatures of 500 °C. The good match between dashed and continuous curves confirm that a single physical simulation test can actually provide insights into laser thermal cycles carried out with the same strategy and treatment speed but with lower peak temperature than that corresponding to the control point.

Physical simulation tests replicating the thermal cycles from Fig. 12 were conducted on new specimens. These specimens were then subjected to hardness and tensile tests.

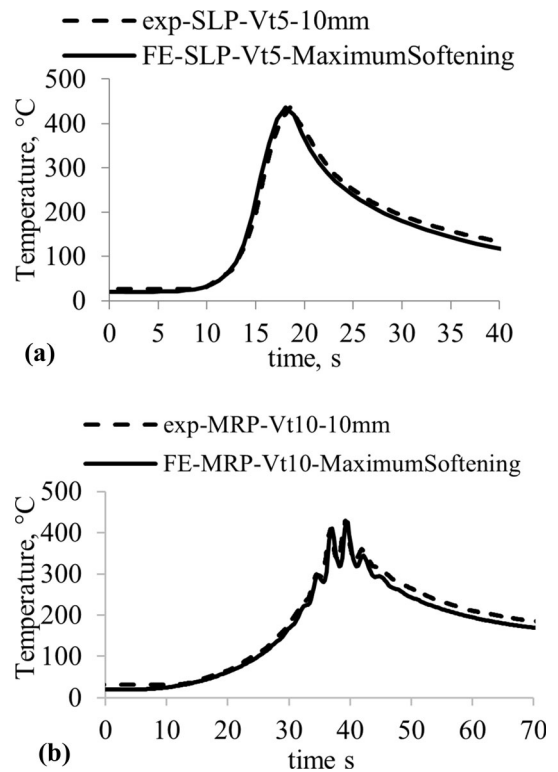


**Fig. 12** Comparison between FE thermal cycles and experimental ones at 10 mm from the specimen center during physical simulation tests at the highest peak temperature for treatments (a) SLP-Vt5 and (b) MRP-Vt10

The hardness test results confirm the occurrence of maximum softening under these conditions. The measured hardness values at the center of these specimens correspond to those observed at the peak temperature of approximately 430 °C in the hardness profiles shown in Fig. 7(b).

The tensile test results are shown in Fig. 13, which include also, for a comparison, the engineering stress-strain data at the supply state, the furnace annealed state, and softening conditions recorded at the peak temperature of 500 °C.

In the maximum softening condition, laser treatments SLP-Vt5 and MRP-Vt10 exhibit lower UTS than the supply state and higher UTS than the furnace annealed state. Moreover, fracture deformability is higher than the supply state but lower than the furnace annealed state.

In the maximum softening condition, compared to softening achieved at a peak temperature of 500 °C, there is approximately a 12% reduction in UTS and a 15% increase in fracture deformability.

The SLP and MRP strategies were compared in terms of peak temperatures distribution and width of the softened area. For this purpose, a grid of points was defined on the surface of the blank within the FE model. The grid had a spacing of 1 mm, both longitudinally and transversely. The peak temperature was calculated at each node of the grid. In the FE model, the equations of the hardness as a function of the peak temperature (Table 7) were implemented with the aim of calculating the hardness in each node of the grid. The hardness data at each node allows for determining the width of the softened region.

Figure 14 displays the peak temperature distribution (Fig. 14a) and the hardness distribution (Figure 14b) on the

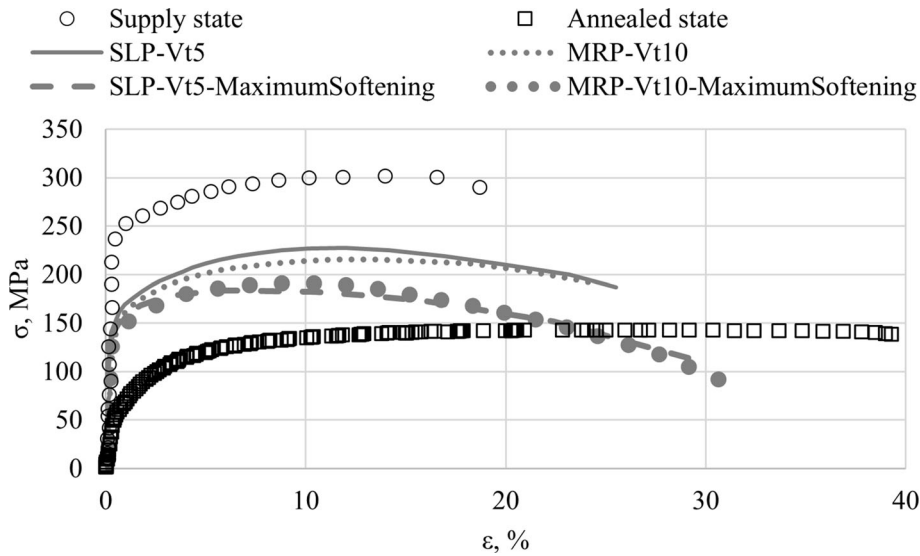


**Fig. 13** Engineering stress-strain curves for specimens in different states: supply state, after furnace annealing, after physical simulation of laser thermal cycles SLP-Vt5 and MRP-Vt10 at a peak temperature of 500 °C, and after physical simulation of laser thermal cycles SLP-Vt5 and MRP-Vt10 at a peak temperature of 430 °C

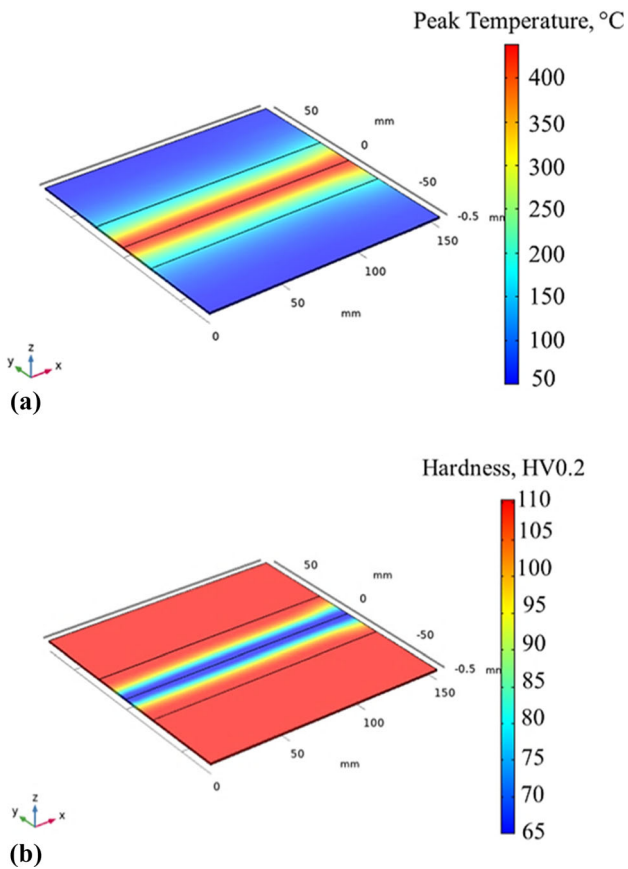


**Fig. 14** Distribution of peak temperature (a) and hardness (b) on the blank under SLP laser heat treatment at  $V_t$  of 5 mm/s in the maximum softening condition ( $T_{peak} = 430$  °C)

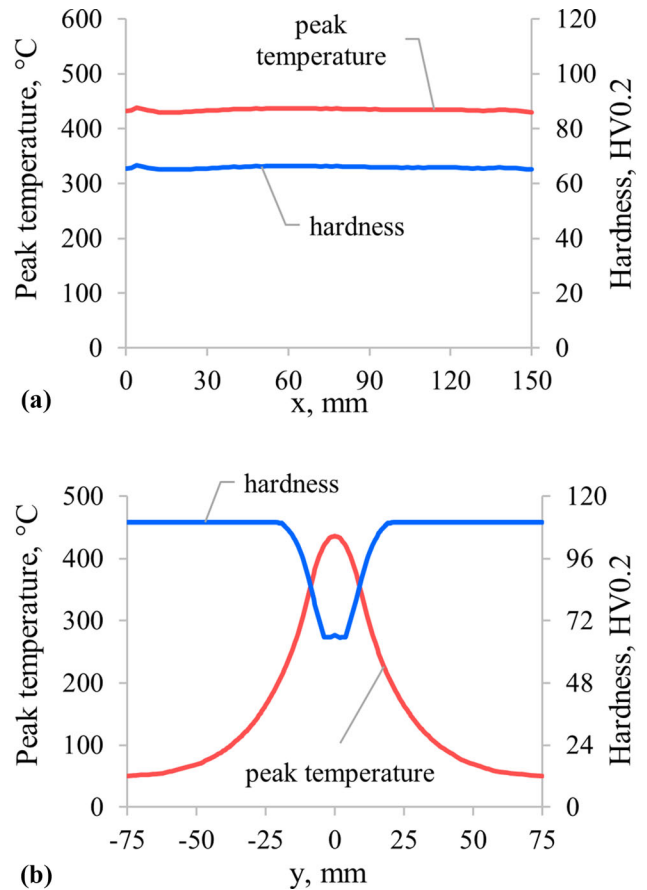


**Fig. 15** Hardness and peak temperature profiles along (a) the longitudinal axis and (b) the transverse axis of the blank subjected to SLP laser treatment at  $V_t = 5$  mm/s under the maximum softening condition ( $T_{peak} = 430$  °C)

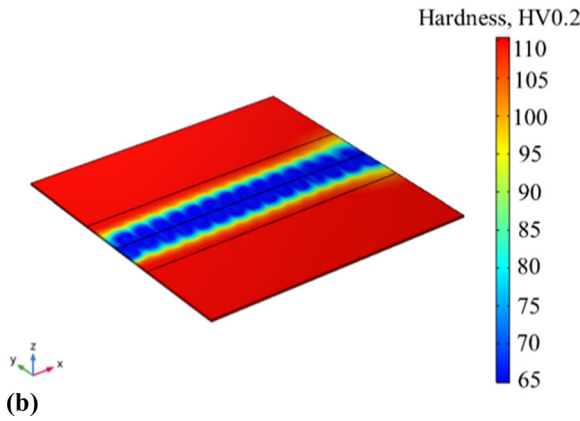
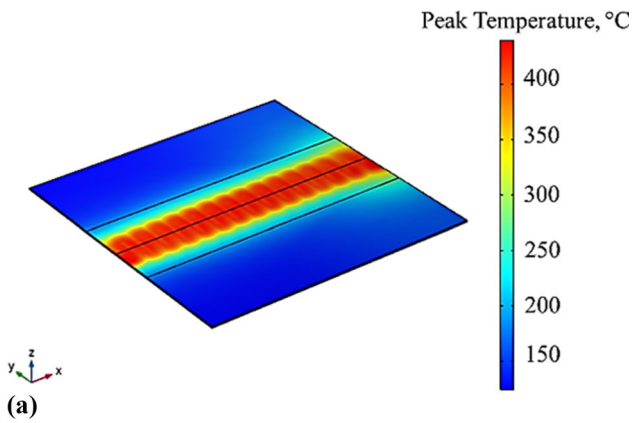


**Fig. 16** Distribution of peak temperature (a) and hardness (b) on the blank under MRP laser heat treatment at  $V_t$  of 10 mm/s in the maximum softening condition ( $T_{peak} = 430^\circ\text{C}$ )

blank under the maximum softening condition for the SLP strategy at  $V_t$  of 5 mm/s.

In Fig. 15, for the same treatment condition, the overlay of the hardness profile and the peak temperature profile is shown along the longitudinal axis (Fig. 15a) and the transverse axis (Fig. 15b).

It can be observed that along the longitudinal axis, there is a quite uniform distribution of peak temperature, resulting in a uniform distribution of the hardness. By examining the results along the transverse axis, the width of the softened area can be determined to be approximately 8 mm.

The distribution of peak temperature and the hardness one on the blank under the maximum softening condition for the MRP strategy executed at  $V_t=10\text{mm/s}$  are shown in Fig. 16(a) and (b), respectively.

By positioning along the longitudinal and transverse axes, it is possible to obtain the profiles of peak temperature and hardness in both directions. These profiles are shown in Fig. 17.

In the MRP strategy, it can be observed that along the longitudinal axis, the peak temperature ranges between a minimum value of  $415^\circ\text{C}$  and a maximum value of  $435^\circ\text{C}$ . As in the SLP strategy, the laser power modulation helps to reduce peak temperature variation along the surface treatment direction but cannot eliminate peak temperature local fluctuations due to the multiple parallel path of the laser. This temperature fluctuation results in a slight variation in hardness along the

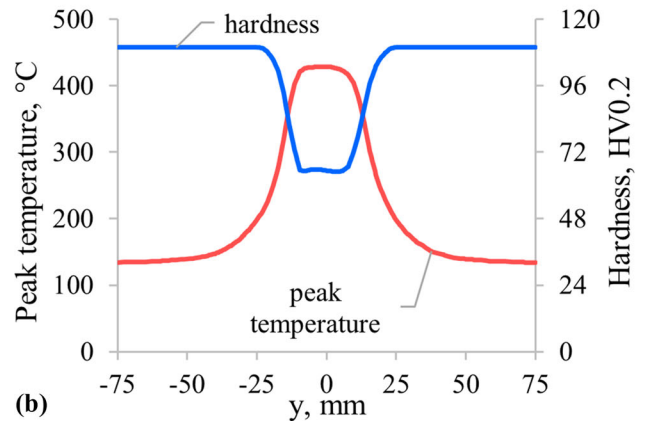
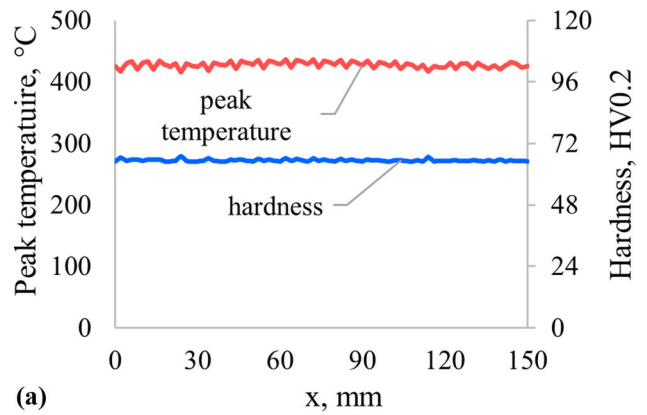


**Fig. 17** Hardness and peak temperature profiles along (a) the longitudinal axis and (b) the transverse axis of the blank subjected to MRP laser treatment at  $V_t = 10\text{ mm/s}$  under the maximum softening condition ( $T_{peak} = 430^\circ\text{C}$ )

longitudinal axis of the blank. Here, the hardness oscillates between a minimum value of 64 HV0.2 and a maximum value of 67 HV0.2. However, this difference can be considered negligible.

To enhance the uniformity of temperature distribution along the longitudinal section of the blank, future developments involve optimizing the overlap between consecutive parallel paths.

The analysis of Fig. 17(b) reveals an approximately 20 mm width of the softened area. Thus, the movement of the laser source along the  $y$ -axis by 20 mm results in the entire region being softened. Comparing the two investigated strategies, MRP strategy offers a larger softened area than SLP one.

## 5. Conclusion

This work investigates the effects of softening in an age-hardenable aluminum alloy after localized laser heat treatment. Specifically, the study evaluates the influence of process parameters such as peak temperature and interaction time, as well as the influence of treatment strategies. Two treatment strategies were examined: one with laser source movement

drawing a single linear path and the other with laser source movement drawing multiple rectangular paths.

This study employed a numerical-experimental methodology, where the experimental part involved physical simulation tests on a laboratory scale. The obtained results reveal the following findings:

- For both investigated strategies, there exists a peak temperature that ensures maximum softening of the alloy. Within the explored range, for a fixed treatment strategy, an increase in interaction time results in a higher peak temperature for maximum softening.
- For both strategies, an increase in interaction time and, consequently, a reduction in treatment speed, results in a higher level of alloy softening.
- The two strategies ensure the same level of softening when their interaction times are comparable.
- Under maximum softening conditions, both investigated treatments show a 37% reduction in UTS and a 58% increase in A compared to the supply state material. However, compared to the material annealed in the furnace, the laser heat treated alloy exhibit a 33% higher UTS and a 25% decrease in A.
- The metallographic analysis conducted through SEM aligns with the findings in the literature, indicating that the maximum softening obtained laser heat treatment around 410–430 °C is due to overaging phenomena. This is corroborated by the identification of  $\beta$  particles in the treated specimens, which exhibit increasing sizes with longer interaction times. Further investigations are planned for the future, involving the use of a TEM to analyze the strengthening precipitates in more detail and establish more precise correlations between process parameters and microstructure.
- Although the two strategies ensure the same level of softening for a comparable interaction time, the MRP strategy allows for a wider softened area compared to that obtained with SLP strategy.

In conclusion, this study reveals that, regardless of the adopted treatment strategy, the key process parameters are the peak temperature during the laser thermal cycle and the interaction time. The innovative aspect that emerges is the significant influence of the chosen treatment strategy on the extent of the softened area with fixed values for interaction time, peak temperature, and the area covered by the laser source remaining constant. Furthermore, this study deduces that, by maintaining equal treatment speeds for both strategies, the approach involving multiple rectangular paths would result in a higher level of softening. This is attributed to the greater interaction times in this last strategy due to the reduction in equivalent speed.

These results provide essential insights for optimizing laser treatment strategies to attain desired material properties during laser heat treatment.

## Acknowledgments

The authors would like to thank Dr. Oleg Mishin and Dr. Matteo Villa from the Technical University of Denmark (DTU), respectively, for the valuable support in metallographic analysis

and for hosting the author Maria Emanuela Palmieri as a visiting researcher at DTU.

## Funding

Open access funding provided by Politecnico di Bari within the CRUI-CARE Agreement. This work was supported by PNRR-Spoke 11 (Innovative Materials and Lightweighting) project and MISE FCS Project F/310302/01-05/X56-"MANAGE5.0."

## Data availability

All data generated or analyzed during this study are included in this published article.

## Competing interests

The authors have no relevant financial or non-financial interests to disclose.

## Open Access

This article is licensed under a Creative Commons Attribution 4.0 International License, which permits use, sharing, adaptation, distribution and reproduction in any medium or format, as long as you give appropriate credit to the original author(s) and the source, provide a link to the Creative Commons licence, and indicate if changes were made. The images or other third party material in this article are included in the article's Creative Commons licence, unless indicated otherwise in a credit line to the material. If material is not included in the article's Creative Commons licence and your intended use is not permitted by statutory regulation or exceeds the permitted use, you will need to obtain permission directly from the copyright holder. To view a copy of this licence, visit <http://creativecommons.org/licenses/by/4.0/>.

## References

1. M. Geiger, M. Merklein, and U. Vogt, Aluminum Tailored Heat Treated Blanks, *Prod. Eng. Res. Devel.*, 2009, **3**, p 401–410
2. A. Kahrimanidis et al., Process Design of Aluminum Tailor Heat Treated Blanks, *Materials.*, 2015, **8**(12), p 8524–8538
3. M. Merklein et al., Tailored Heat Treated Profiles-Enhancement of the Forming Limit of Aluminum Profiles Under Bending Load, *Key Eng. Mater.*, 2012, **4**(504), p 375–380
4. Fröck, H. et al. Precipitation Behaviour and Mechanical Properties During Short-Term Heat Treatment for Tailor Heat Treated Profiles (THTP) of Aluminium Alloy 6060 T4. *Materials Science Forum*. Vol. 877. Trans Tech Publications Ltd, 2017
5. M. Merklein, W. Böhm, and M. Lechner, Tailoring Material Properties of Aluminum by Local Laser Heat Treatment, *Phys. Proced.*, 2012, **39**, p 232–239
6. K. Alexander, W. Daniel, and M. Marion, Influence of a Short Term Heat Treatment by Conduction and Induction on the Mechanical Properties of AA6014 Alloys, *Phys. Proced.*, 2014, **56**, p 1410–1418
7. R. Pereira et al., An Experimental and Numerical Study on Aluminum Alloy Tailor Heat Treated Blanks, *J. Manuf. Mater. Process.*, 2023, **7**(1), p 16
8. M. Picc et al., Laser alloying with WC Ceramic Powder in Hot Work Tool Steel using a High Power Diode Laser (HPDL), *Adv. Mater. Res.*, 2007, **15**, p 193–198
9. L.A. Dobrzański et al., Laser Surface Treatment of Multicrystalline Silicon for Enhancing Optical Properties, *J. Mater. Process. Technol.*, 2008, **201**(1–3), p 291–296
10. M. Graser et al., Application of Tailor Heat Treated Blanks Technology in a Joining by Forming Process, *J. Mater. Process. Technol.*, 2019, **264**, p 259–272

11. Peixinho, N., et al. Development of Laser Heat Treatment Process for Assisted Forming of Aluminum Alloys. 2021 6th International Conference on Smart and Sustainable Technologies (SpliTech). IEEE, (2021)
12. A. Hetzel, M. Merklein, and M. Lechner, Enhancement of the Forming Limits for Orbital Formed Tailored Blanks by Local Short-Term Heat Treatment, *Proced. Manuf.*, 2020, **47**, p 1197–1202
13. S. Zarini et al., Formability Enhancement of Al 6060 Sheets Through Fiber Laser Heat Treatment, *Int. J. Mater. Form.*, 2017, **10**, p 741–751
14. Poznak, A., Daniel F., and Paul S. Automotive Wrought Aluminium Alloys. “ Fundamentals of Aluminium Metallurgy. Woodhead Publishing, pp. 333-386. (2018)
15. H. Fröck et al., A Phenomenological Mechanical Material Model for Precipitation Hardening Aluminium Alloys, *Metals*, 2019, **9**(11), p 1165
16. M. Graser, N. Pflaum, and M. Merklein, Influence of a Local Laser Heat Treatment on the Bending Properties of Aluminium Extrusion Profiles, *Proced. CIRP*, 2018, **74**, p 780–784
17. N. Rigas and M. Merklein, Numerical and Experimental Investigations for Distortion-Reduced Laser Heat Treatment of Aluminum, *Prod. Eng. Res. Devel.*, 2021, **15**, p 479–488
18. M.E. Palmieri, V.D. Lorusso, and L. Tricarico, Laser-Induced Softening Analysis of a Hardened Aluminum Alloy by Physical Simulation, *Int. J. Adv. Manuf. Technol.*, 2020, **111**, p 1503–1515
19. A. Mohammadi et al., Bending Properties of Locally Laser Heat Treated AA2024-T3 Aluminium Alloy, *Phys. Proced.*, 2012, **39**, p 257–264
20. N. Rigas and M. Merklein, Experimental Investigation of Distortion Behavior of Laser Heat Treated Blanks, *Proced. CIRP*, 2020, **94**, p 557–560
21. M.E. Palmieri and L. Tricarico, Physical Simulation of Laser Surface Treatment to Study Softening Effect on Age-Hardened Aluminium Alloys, *J. Manuf. Mater. Process.*, 2022, **6**(3), p 64
22. E. Liverani et al., Development of a Model for the Simulation of Laser Surface Heat Treatments with use of a Physical Simulator, *J. Manuf. Process.*, 2017, **26**, p 262–268
23. A. Piccininni and G. Palumbo, Design and Optimization of the Local Laser Treatment to Improve the Formability of Age Hardenable Aluminium Alloys, *Materials*, 2020, **13**(7), p 1576
24. A. Piccininni and G. Palumbo, Numerical Modelling of the Annealing Determined by Short-Term Laser Treatment Using a Physical Simulation-Based Approach, *CIRP J. Manuf. Sci. Technol.*, 2023, **45**, p 210–224
25. Available on <https://www.ambrogicolombo.it/product/alluminio-en-a-w-6082/>
26. COMSOL Multiphysics 5.6. COMSOL Multiphysics Reference Manual. Burlington, MA: COMSOL
27. R. Weber et al., Short-Pulse Laser Processing of CFRP, *Phys. Proced.*, 2012, **39**, p 137–146
28. D. Abolhasani et al., A Double Raster Laser Scanning Strategy for Rapid Die-Less Bending of 3D Shape, *J. Mater. Res. Technol.*, 2019, **8**(5), p 4741–4756
29. J. Cheng et al., Review of Techniques for Improvement of Softening Behavior of Age-Hardening Aluminum Alloy Welded Joints, *Materials*, 2021, **14**(19), p 5804
30. M. Jula, R. Dehmolaei, and K. Ranjbar, Softening, Hardening, and Precipitation Evolution of the AA6082-T651 Heat-Affected Zone Caused by Thermal Cycles During and After Welding, *Metals Mater. Int.*, 2023, **29**(12), p 3664–3678
31. T. Ma and G. Den Ouden, Softening Behaviour of Al-Zn-Mg Alloys Due to Welding, *Mater. Sci. Eng. A*, 1999, **266**(1–2), p 198–204
32. Y. Liang et al., Effect of TIG Current On Microstructural And Mechanical Properties of 6061-T6 Aluminium Alloy Joints by TIG-CMT Hybrid Welding, *J. Mater. Process. Technol.*, 2018, **255**, p 161–174
33. O.R. Myhr, Ø. Grong, and S.J. Andersen, Modelling of the Age Hardening Behaviour of Al-Mg-Si Alloys, *Acta Mater.*, 2001, **49**(1), p 65–75
34. O.R. Myhr et al., Modelling of the Microstructure and Strength Evolution in Al-Mg-Si Alloys During Multistage Thermal Processing, *Acta Mater.*, 2004, **52**(17), p 4997–5008
35. N. Kumar et al., Effect of Cryorolling and Annealing on Recovery, Recrystallisation, Grain Growth and their Influence on Mechanical and Corrosion Behaviour of 6082 Al alloy, *Mater. Chem. Phys.*, 2015, **165**, p 177–187
36. H.Q. Wang, W.L. Sun, and Y.Q. Xing, Microstructure Analysis on 6061 Aluminum Alloy after Casting and Diffuses Annealing Process, *Phys. Proced.*, 2013, **50**, p 68–75
37. Z. Zhang et al., Effects of Combined Pre-Straining and Pre-Aging on Natural Aging and Bakehardening Response of an Al-Mg-Si Alloy, *Acta Metall. Sinica Eng. Lett.*, 2013, **26**, p 340–344

**Publisher's Note** Springer Nature remains neutral with regard to jurisdictional claims in published maps and institutional affiliations.